Journal of Zhejiang University-SCIENCE A 2026 27(1):26-42
www.jzus.zju.edu.cn; www.springer.com/journal/11582
E-mail: jzus_a@zju.edu.cn

Research Article
https://doi.org/10.1631/jzus.A2500044

Comparative analysis of windbreak configurations for unloaded gondola train cars under crosswinds based on computational fluid dynamics and multi-body dynamics

Jiayuan SONG, Wentao HE, Yanlin HU, Kaiyun WANG✉

State Key Laboratory of Rail Transit Vehicle System, Southwest Jiaotong University, Chengdu 610031, China

Abstract: Understanding the aerodynamic and dynamic characteristics of unloaded freight trains in crosswinds is pivotal for ensuring their operational safety and reliability. The dynamic performance of unloaded gondola cars under varying windbreak heights is therefore investigated in this study, revealing distinct differences in lateral stability and safety indicators, and enabling the determination of an optimal windbreak height. A 3D unsteady aerodynamic model was developed using the improved delayed detached eddy simulation (IDDES) method and an overset numerical mesh. Also leveraging a multi-body dynamics (MBD) model of a three-wagon freight car configuration, we investigate time-averaged aerodynamic forces, transient flow field distributions, and nonlinear dynamic responses. Parametric analyses reveal a non-monotonic relationship between the height of the windbreak and the stability of the train. A windbreak with a critical height of 2 m (0.74 relative to the car body height) results in 76%, 64%, and 81% lower values of the derailment coefficient C_D, wheel unloading ratio R, and overturning coefficient C_O, respectively. Notably, when the height of the windbreak exceeds 2 m, vortices within the gondola induce an adverse pressure coefficient distribution (C_p=−2.17) on the leeward internal wall, intensifying the lateral force and overturning moment. Furthermore, frequency-domain analysis reveals that the lateral sway and overturning vibration mode are associated with low-frequency (1.61 Hz) lateral vibrations under crosswind conditions. This study provides a theoretical foundation for the design and optimization of railway windbreaks.

Key words: Crosswind; Train gondola; Unsteady aerodynamics; Dynamic response; Train safety; Windbreaks

1 Introduction

Heavy haul freight trains play a crucial role in coal transportation in Northwest China, helping ensure energy supply security. These trains, which are characterized by lengthy formations and extensive running lines, are particularly vulnerable to strong wind conditions. When subjected to strong crosswinds, the lateral force and overturning moment on the train increase substantially, thereby compromising the safety of operations (Andersson et al., 2004; Tian, 2015). Freight trains are susceptible to strong crosswinds when operating in an unloaded state. The associated aerodynamic loads can cause the empty containers to overturn and fall, increasing the risk of incidents such as derailment and train overturning (Raib, 2009; Liu et al., 2022).

Extensive research has investigated the aerodynamics of crosswinds and windbreaks. At present, wind tunnel experiments, dynamic train model testing, and numerical simulations are the primary approaches for investigating train aerodynamics (Li et al., 2024; Pan et al., 2025). Wind tunnel tests (Suzuki et al., 2003) have revealed that the aerodynamic characteristics of trains in crosswinds are influenced not only by the shape of the vehicle but also by its surrounding infrastructure, such as bridges, embankments, and tunnels (Hu et al., 2025). Railway embankments positioned on the windward side tend to lift and accelerate crosswind airflow, deteriorating the aerodynamic performance of the train (Cheli et al., 2010; Gao and Li, 2011; Noguchi et al., 2019). Gao et al. (2024, 2025) employed the Reynolds-averaged Navier-Stokes (RANS) method to investigate the impact of windbreaks on crosswind

✉ Kaiyun WANG, kywang@swjtu.edu.cn
Kaiyun WANG, https://orcid.org/0000-0003-0958-4260

Received Feb. 15, 2025; Revision accepted June 13, 2025;
Crosschecked Dec. 1, 2025; Online first Jan. 6, 2026

airflow and train stability in complex terrains. Zhou et al. (2023) explored the spatiotemporal evolution of eddies and pressure distributions on a train's surface under crosswind conditions. To improve the aerodynamic performance of trains, some scholars have investigated different types of windbreaks and geometric parameters, and proposed optimized configurations. For instance, Hashmi et al. (2019) noted that windbreaks created a lower pressure distribution on the surface of the model train due to shielding effects. Yang et al. (2021) found that increasing the windbreak by just one meter can effectively reduce the horizontal wind speeds. Simulation of the dynamic passage of the train through windbreaks indicated that a single windbreak on the windward side can effectively resist strong crosswinds, while also reducing the cost of construction (Niu et al., 2022; Zhang et al., 2024).

Differing types of windbreaks, such as porous, solid, or slope-type windbreaks, also influence the operational performance of trains. Utilizing the Lattice Boltzmann method, Mohebbi et al. (2019, 2025) examined the effects of windbreak height, slope, and porosity on aerodynamic force coefficients, and concluded that windbreaks with a porosity level of 15% offer superior wind-mitigating performance. Moreover, Xue et al. (2025) applied the improved delayed detached eddy simulation (IDDES) method to simulate a 1/8 scale train model under solid windbreaks of varying heights. Zhao et al. (2024) investigated the aerodynamic behavior of high-speed trains traversing diverse terrains and windbreak types, revealing that windbreaks can effectively alleviate the aerodynamic disturbances often experienced in transition zones.

Flow separation is more prominent on the surfaces of freight train compartments than on passenger trains. To accurately capture the complex flow field characteristics around freight vehicles, researchers have employed various predictive turbulence models. Aerodynamic loads on a train can be influenced by various configurations, including the gaps between adjacent freight cars. Maleki et al. (2020) revealed the flow mechanism over the roof and leeward side of train container cars, while considering variations in the flow topology between adjacent cars due to unstable flow. Also, Maleki et al. (2017) evaluated the performance of turbulent methods such as embedded large eddy simulation (ELES), scale-adaptive simulation (SAS), unsteady Reynolds-averaged Navier-Stokes (URANS), and RANS in capturing the flow around freight cars, concluding that the ELES method most accurately models flow separation.

Dynamics tests and multi-body dynamics (MBD) simulations are the primary methods for studying the stability and safety of train operations. Researchers have numerically calculated the dynamic responses of freight trains under crosswinds based on aerodynamic loads. The risk of overturning can then be evaluated, informing improved speed limits under crosswinds (Zhang et al., 2023; Wen et al., 2024). Field tests in another study measured the wheel–rail forces of trains passing through windbreaks of varying lengths under a 32 m/s crosswind, clarifying the dynamic mechanism of train creeping caused by gaps in the windbreak, and revealing that the sudden increase in transient aerodynamic loads is the fundamental cause of this phenomenon (Sun et al., 2019, 2020). Additionally, Li et al. (2025) demonstrated that frequencies closer to the suspension vibration mode frequencies under unsteady aerodynamic loads can cause greater vibration of the train.

Most previous studies have focused on box cars (Flynn et al., 2016), container freight cars (Quazi et al., 2023), and passenger trains (Niu et al., 2018), and optimized the shapes of new trains to adapt to strong crosswinds (Zhang et al., 2011). However, research on gondolas (open-top cars) in unloaded states remains relatively scarce. The key differences between unloaded freight trains and passenger trains in terms of aerodynamic stability and dynamic behavior can be summarized in three main aspects:

1. Aerodynamic flow characteristics: Unloaded freight trains, especially those with open-top gondola cars, exhibit significantly different airflow patterns than passenger trains.

2. Structural and dynamic complexity: Heavy-duty freight trains include unique structural elements such as bolsters, wedges, and load-bearing saddles. These components contribute to increased nonlinearities in their MBD models.

3. Track irregularity sensitivity: Freight trains, particularly when heavily loaded or operating on long-haul routes, often experience poorer track conditions than passenger trains, and unloaded freight cars tend to be more susceptible to the effects of track irregularities.

In this study, the variation law of aerodynamic load is elucidated by analyzing the flow field structure

surrounding train gondolas. Additionally, the influencing mechanism of different windbreak heights on the aerodynamic load and nonlinear dynamic response of the freight train is revealed. Our findings can serve as a reference when constructing windbreaks on freight or mixed passenger–freight railway lines.

2 Numerical method

In real railway operations, wagons are typically arranged in groups of three, connected by two drawbars within the group and coupled at each end to adjacent groups. A typical 10000-t train is comprised of 108 wagons. Due to computational constraints, our simulations are conducted using a simplified three-wagon configuration, and in the MBD simulation, the coupler is modeled in a simplified form. The aerodynamic loads derived from computational fluid dynamics (CFD) simulations are applied to the MBD model as external excitations.

2.1 Aerodynamic model

2.1.1 Geometric description

The typical formation for a heavy haul train consists of C80-type gondolas hauled by HXD1 electric locomotives. In actual operations, a long train formation with the three-wagon composition configuration would be employed. To mitigate the impact of wake flow on the third gondola (Golovanevskiy et al., 2012; Liang et al., 2023) while also conserving computational resources, a geometric model comprising one HXD1 electric locomotive and four C80-type gondolas is employed in this study for aerodynamic simulations. The three-wagon composition configuration model is selected for the dynamic simulations. Fig. 1 illustrates the simplified model of the train and railway embankment, where the complex geometric shapes of the C80-type gondola and the locomotive have been simplified, and the equipment at the rear of the gondolas has been ignored. The gondola body has dimensions of 10.97 m in length (L), 2.7 m in height (H), and 3.23 m in width (W). The gap between each gondola section is 0.8 m, and the length of the locomotive is 20 m. The dimensions of the embankment are determined based on previous studies and railway standards (NRA, 2016, 2017; Niu et al., 2022). The reference plane for the aerodynamic simulation is the top surface of the embankment. The windward side windbreak is set to be 4.45 m from the centerline of the embankment, and its base is 0.87 m below the reference plane. The steel rail structure is neglected, and the height of the train running surface

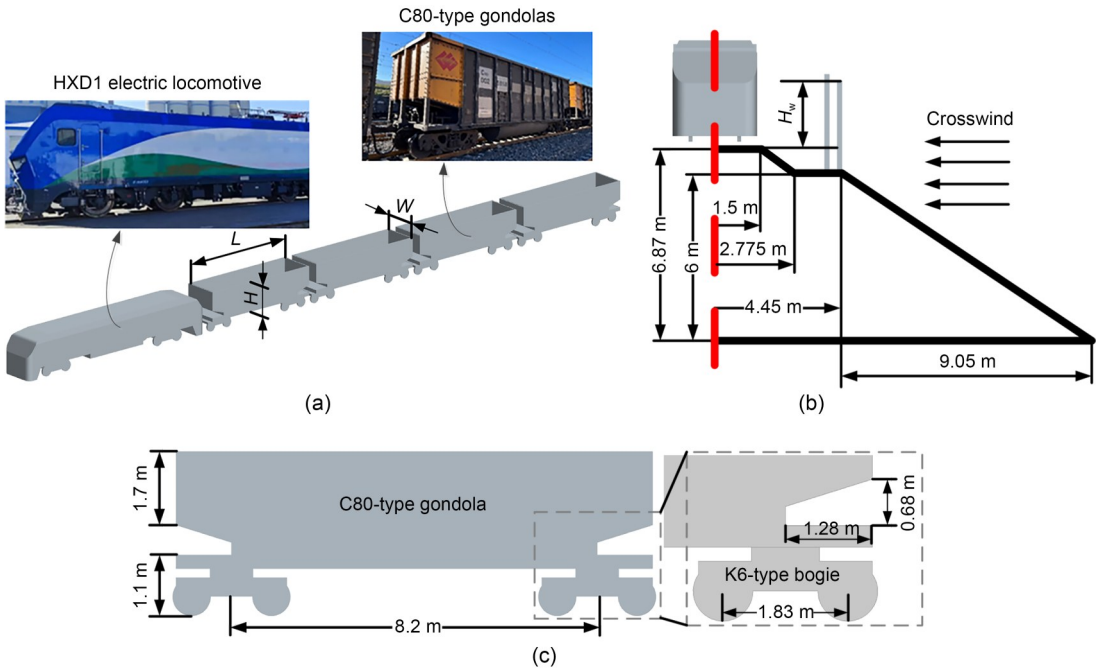

Fig. 1 Dimensions of the vehicles and embankment: (a) simplified model of the heavy haul train; (b) dimensions of the embankment; (c) dimensions of the C80-type gondola

was set to 0.375 m. Referring to practical railway limits and previous studies, windbreaks with heights of 1 m, 2 m, and 3 m were often used for comparative studies (Mohebbi and Rezvani, 2019). When the height of the windbreak is insufficient, it causes an increase in the train overturning moment. Therefore, in this study, we use the height of the windbreak with the minimum overturning moment (Gao and Duan, 2011). The effective heights of the windbreaks (H_w) are defined as 0 m, 1.5 m, 2 m, 3 m, and 4 m. The relative heights (H_w/H) are 0, 0.56, 0.74, 1.11, and 1.48.

2.1.2 Numerical model

Since the Mach number of the flow field around the train is significantly less than 0.3, the compressibility of air can be neglected in the numerical simulation, in keeping with previous research (Li et al., 2023). The differential form of the 3D unsteady incompressible Navier-Stokes equations is (Moukalled et al., 2016):

$$\frac{\partial \rho}{\partial t}+\nabla\cdot(\rho u)=0, \tag{1}$$

$$\rho\frac{\partial u}{\partial t}+\rho u\cdot\nabla u=-\nabla p+\nabla\tau+S, \tag{2}$$

where u, ρ, t, p, τ, and S are the air velocity, density, time, pressure, shear stress, and source term, respectively.

A 3D unsteady incompressible numerical model was established based on the governing equations. The shear stress transport (SST) k-ω model and the IDDES method (Menter, 1994; Shur et al., 2008) were employed. The RANS method has a few limitations in capturing flow field features, such as flow separation and eddy structures (Li et al., 2019). The IDDES method is a hybrid RANS-LES (large eddy simulation) method that captures small-scale flow separation and vortices. In the IDDES method, the delayed detached eddy simulation (DDES) method is used in the eddy region, while the wall function model of the LES method (WMLES) is used in the near-wall region to capture the development of the boundary layer (Wang et al., 2021). The specific formula for the IDDES method is given in the electronic supplementary materials (ESM).

The IDDES method provides improved resolution of vortex structures and more accurately captures turbulence features near the wall. It is thus widely applied in train aerodynamic simulations (Guo et al., 2021; Dai et al., 2024). The second-order unsteady flow is used to solve the governing equations, with the time discretization format of second-order being implicit. The time step was set to 5×10^{-4} s, and the residuals of all physical quantities were maintained at the order of 10^{-5}. The total simulation time of the train's motion was 6 s.

The computational domain has dimensions of 41L in length, 15.5L in width, and 5.2L in height, as shown in Fig. 2; the embankment is situated 8.8L from the leeward outlet. To ensure the flow field around the train is stable when the train enters the region behind the windbreak, the locomotive is initially positioned 2.7L away from the windbreak. The total length of the windbreak is 18.2L. The direction of the train's movement is along the $+x$ direction, and the incoming crosswind is along the $-y$ direction.

The numerical boundary conditions are defined as follows. The train has a constant speed of 80 km/h. The front plane (inlet 1) and the windward side plane (inlet 2) are set as velocity inlets. Given that the average value and fluctuation amplitude of the aerodynamic load increase with the crosswind angle (Zhuang and Lu, 2015), the most difficult operating conditions for the train are simulated by setting the windward angle to 90° (He et al., 2025) and the crosswind velocity to 30 m/s. The leeward side plane (outlet 1) and the rear plane (outlet 2) are specified as pressure outlets with zero pressure. The top plane (top) is defined as a symmetric plane, and the

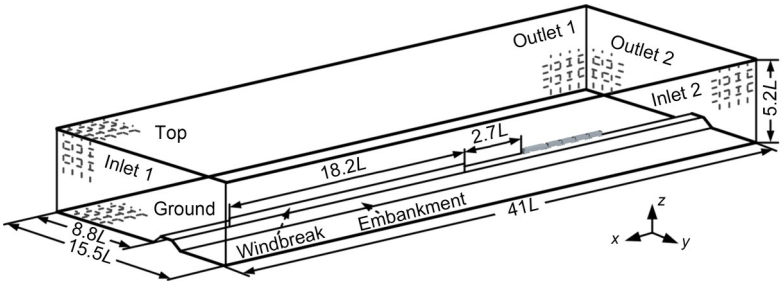

Fig. 2 Aerodynamic computational domain and boundary conditions

surfaces of the train, windbreak, and ground (ground) are specified as walls with no relative velocity. The initial pressure within the computational domain is set to 1 atm (101325 Pa), and the initial temperature is 288.15 K.

2.1.3 Numerical mesh strategy

Overset mesh technology is employed to simulate the train's movement, allowing for data exchange between the overlapping region mesh and background region mesh; this effectively reduces the overall mesh quantity. Fig. 3a illustrates the mesh in the overlapping region and the background region of the y=0 cross-section. An unstructured hybrid mesh is applied, consisting of a trimmer-hexahedral mesh and a prism layer mesh. The minimum size of the overlapping grid units is 160 mm, meeting the overset timestep requirement of t<0.00178 s (Hu et al., 2021), and ensuring the Courant number remains below 1. To capture the flow characteristics near the walls of the train, embankment, and windbreak, a 12-layer boundary-layer mesh with a growth rate of 1.2 is applied. The first layer of the boundary layer has a thickness of 0.06 mm, ensuring that the wall y^+ is close to 1 (Fig. 3c). The basic size and the minimum size of the surface mesh on the train are set to 80 mm and 20 mm, respectively. The surface mesh on the embankment is further refined with the size of the minimum surface mesh set to 40 mm. Considering the complex aerodynamic phenomena on the leeward side of the flow field, local refinement is performed. To ensure a smooth transition between mesh sizes, the basic sizes of refinement boxes 1, 2, and 3 are defined as 640 mm, 320 mm, and 160 mm, with widths of 32 m, 26 m, and 9 m, respectively.

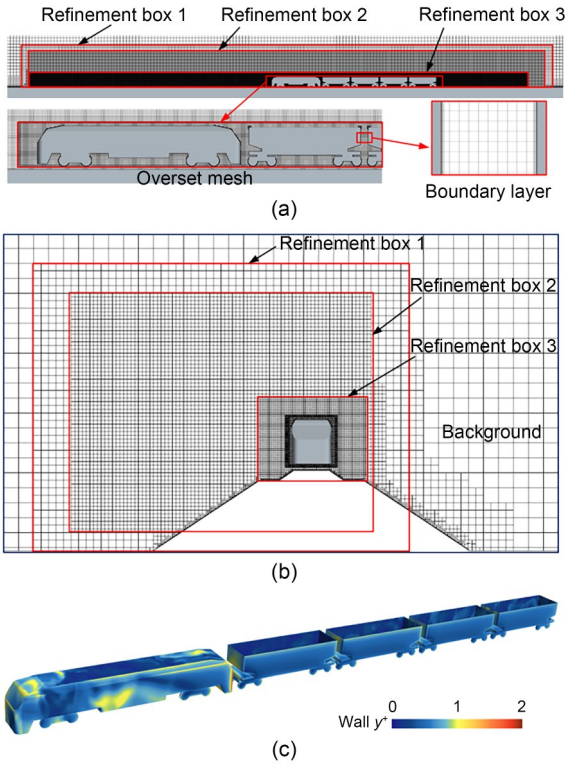

Fig. 3 Computational domain meshing: (a) mesh on the y=0 cross-section and boundary layer; (b) mesh on the transverse section; (c) distribution of the wall y^+

2.2 Multi-body dynamics model

To analyze the dynamic characteristics of the C80-type gondola under unsteady aerodynamic loads, a three-wagon composition model of the C80-type gondolas was developed using SIMPACK dynamics simulation software (Ge et al., 2022), as shown in Fig. 4. The model primarily contains three C80-type gondolas and a traction rod-buffer system. The coupler between the locomotive and the wagon was simplified. A nonlinear stiffness-damping unit is used to simulate the lateral and vertical constraints of the locomotive on the wagon. Moreover, Chinese LM-type wheels and Federal Railroad Administration (FRA) class 5 track irregularities are adopted in the model. The sub-model of the single wagon consists of the car body, bolster, side frame, drawbar, axle box bearing saddle, wheelset, and primary and secondary suspensions, with a total of 74 degrees of freedom (DOFs).

The aerodynamic loading point is positioned at the center of mass of the vehicle. Based on D'Alembert's principle, the vibration equation for each vehicle model can be expressed as:

$$\boldsymbol{M}_{vi}\ddot{\boldsymbol{X}}_{vi}+\boldsymbol{C}_{vi}\dot{\boldsymbol{X}}_{vi}+\boldsymbol{K}_{vi}\boldsymbol{X}_{vi}=\boldsymbol{F}_{vi}, \tag{3}$$

where $\boldsymbol{M}_{vi}$, $\boldsymbol{C}_{vi}$, and $\boldsymbol{K}_{vi}$ are the mass matrix, damping matrix, and stiffness matrix of the ith vehicle, respectively, and $\ddot{\boldsymbol{X}}_{vi}$, $\dot{\boldsymbol{X}}_{vi}$, and $\boldsymbol{X}_{vi}$ are the acceleration vector, velocity vector, and displacement vector, respectively. $\boldsymbol{F}_{vi}$ is the excitation force vector received by the ith vehicle, including gravity, coupler forces, wheel–rail forces, and aerodynamic load.

In the sub-model of the wagon, the body, side frame, drawbar, and wheelset are defined as 6-DOF rigid bodies; the axle box bearing saddle has one pitch DOF relative to the wheelset. The wedge suspension system model mainly includes a bolster, wedge, column

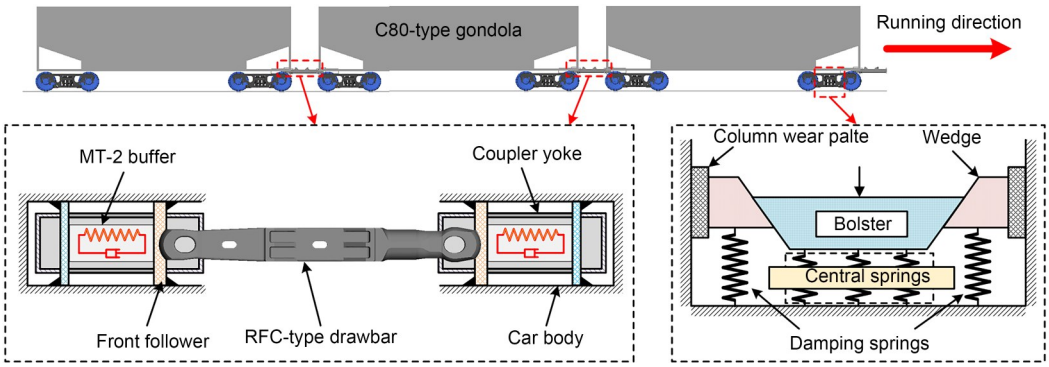

Fig. 4 Three-wagon composition model of the C80-type gondolas

wear plate, center spring, and damping spring. The bolster has two DOFs relative to the body, including the heave and pitch; the wedge has one heave DOF. The drawbar-buffer model primarily includes the MT-2 buffer, front follower, rod-fixed coupler (RFC)-type drawbar, coupler yoke, and coupler box connected with the car body. The drawbar has four DOFs: roll, pitch, yaw, and extension; the front follower has one extension DOF. Each wagon experiences aerodynamic loads, including drag force (F_x), lateral force (F_y), lift force (F_z), rolling (overturning) moment (M_x), pitch moment (M_y), and yaw moment (M_z) when under the crosswind. The main parameters of the dynamics model are shown in Table S1 of the ESM.

The vibration mode characteristics of the MBD system, obtained through solution of the eigenvalues, are summarized in Table 1. Analysis of the vibration mode parameters reveals distinct frequency segregation between different motion types. For instance, considering the car body, the frequencies of the lateral sway (1.33 Hz and 1.46 Hz), overturning (2.10 Hz), and yaw (16.09 Hz) are lower. In contrast, vibration modes associated with vertical motion, such as bounce (20.73 Hz) and pitch (26.35 Hz), display comparatively higher frequencies.

Table 1 Vibration mode types and numerical frequencies of the MBD system

Item	Vibration mode type	Numerical frequency (Hz)
Car body	Lateral sway and overturning	1.33
	Lateral sway and overturning	1.46
	Overturning	2.10
	Longitudinal sway	5.90
	Yaw	16.09
	Bounce	20.73
	Pitch	26.35
Wheelset	Lateral sway and yaw	1.76
	Lateral sway and yaw	1.85
Bogie	Overturning	2.60
	Longitudinal sway	4.49

3 Validation

3.1 Mesh independence analysis

Due to the small range of variation in the height of the windbreak, the difference in mesh quantities for varying conditions is less than 1%. Four sets of meshes with base sizes of 0.9 m, 1.0 m, 1.1 m, and 1.2 m were established. Table 2 presents the relative errors of aerodynamic drag and aerodynamic side force for different meshes. Compared to the fine mesh, the errors for Mesh 1, Mesh 2, and Mesh 3 of the drag are 8.92%, 4.58%, and 3.56%, while the errors of the lateral force are 18.35%, 3.79%, and 0.19%, respectively. Consequently, the aerodynamic results from the Mesh 3 converged, and its calculation accuracy is close to the fine mesh. Considering computational costs and precision, Mesh 3 is chosen to investigate the aerodynamic performance of trains under crosswinds.

3.2 Aerodynamic verification of the double-stacked container wagon

Li et al. (2017) conducted wind tunnel tests on double-stacked container wagons, at a scale of 1:14.6 and with an incoming wind speed of 30 m/s; we match this crosswind speed in our study. The Reynolds number of the incoming flow was 0.3×10^6, and the geometric dimensions of the test wagon were $L\times W\times H$=1000 mm×438 mm×171 mm. A total of 49 different combinations

Table 2 Relative errors of aerodynamic forces for meshes of different precision

Mesh	Basic size (m)	Overset mesh	Total number of mesh	Mean F_x (N)	Relative error of F_x (%)	Mean F_y (N)	Relative error of F_y (%)
Mesh 1	1.2	4.59×10^6	2.05×10^7	−4276	8.92	−50851	18.35
Mesh 2	1.1	5.78×10^6	2.73×10^7	−3746	4.58	−59915	3.79
Mesh 3	1.0	6.64×10^6	3.07×10^7	−4066	3.56	−62160	0.19
Mesh 4	0.9	7.54×10^6	3.44×10^7	−3926	–	−62277	–

of gaps were tested in the wind tunnel. The condition with a front gap (G_f) of 3.23W and a base gap (G_b) of 0.3W was selected for validation. The model was placed above a false floor with a ground clearance of 28 mm, which is equivalent to the radius of a full-scale 410 mm wheel. All instrumentation was installed on the test wagon, which was positioned fourth in the train formation. Additionally, all extra inter-wagon gaps were sealed to isolate the influence of G_f and G_b, thereby minimizing the effects of upstream gap interactions and maintaining controlled experimental conditions.

The simulation employed the IDDES method, with a 20-layer boundary layer mesh and a total thickness of 8 mm. The maximum value of the wall y^+ was 1.05, and the time step was defined as $0.006T_{ref}$, where T_{ref} represents the time of the flow passing over one wagon length at the freestream velocity. Fig. 5 shows a comparison of the IDDES method, ELES method (Maleki et al., 2019), and the test results. In ELES, the random 2D vortex method (VM) was employed at the inlet to produce a velocity disturbance. Velocity perturbations at the boundary are in fact not considered in IDDES, which may cause errors in predicting flow separation. The results indicate that the IDDES method accurately predicts the flow field near the upstream positive pressure region and the downstream point c, with

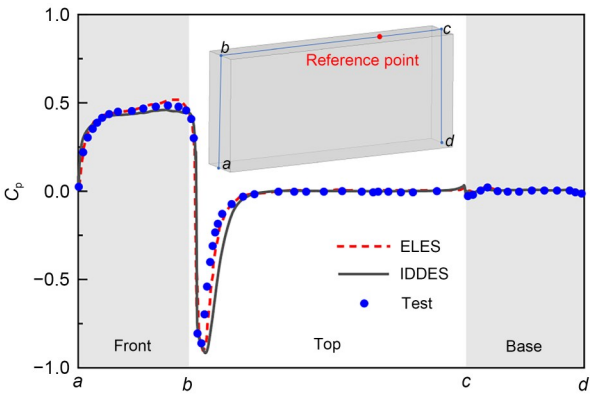

Fig. 5 Surface pressure coefficient (C_p) on the monitoring line of the simulation and the wind tunnel test

a maximum error of 5.3% compared to the test. However, the IDDES method predicts the position of the maximum negative pressure point in the flow separation region to be slightly downstream. The maximum errors in pressure gradient predicted by the IDDES and ELES methods are 6.2% and 4.1%, respectively. Given the balance between precision and computational cost, the IDDES method effectively meets the accuracy requirements and captures the flow characteristics around the train.

3.3 Dynamic validation of the heavy haul train

In a 2023 field test, the dynamic responses of a 20000-t heavy haul train passing through various sections were monitored. Since the track section in this study was straight, and had smaller acceleration fluctuations, the lateral acceleration of the 107th wagon was selected for the validation of the dynamic model, as shown in Fig. 6a. Acceleration sensors were installed at the end of the car body, enabling monitoring of the longitudinal, lateral, and vertical accelerations. The sampling frequency in the test was set at 1000 Hz, and the train traversed the straight section at a constant speed of 60 km/h. In the simulation, FRA class 5 track irregularities were used as an external excitation. All subsequent numerical calculations used the same track irregularity as in the validation. Fig. S2 of the ESM shows the track irregularities and the experimentally segmented data following 0.4–15 Hz bandpass filtering.

Figs. 6b and 6c present the simulation results of the three-wagon composition model compared with the test. It can be observed that during the straight section, both the test and simulated acceleration amplitudes fluctuated between −0.3 and 0.3 m/s^2, showing strong agreement. Additionally, frequency-domain analysis reveals that the vehicle vibration falls within two main frequency ranges. The low-frequency (1.27–3.55 Hz) vibration data were calculated more accurately. However, due to discrepancies between the simulated and measured values of track irregularities, noticeable errors are

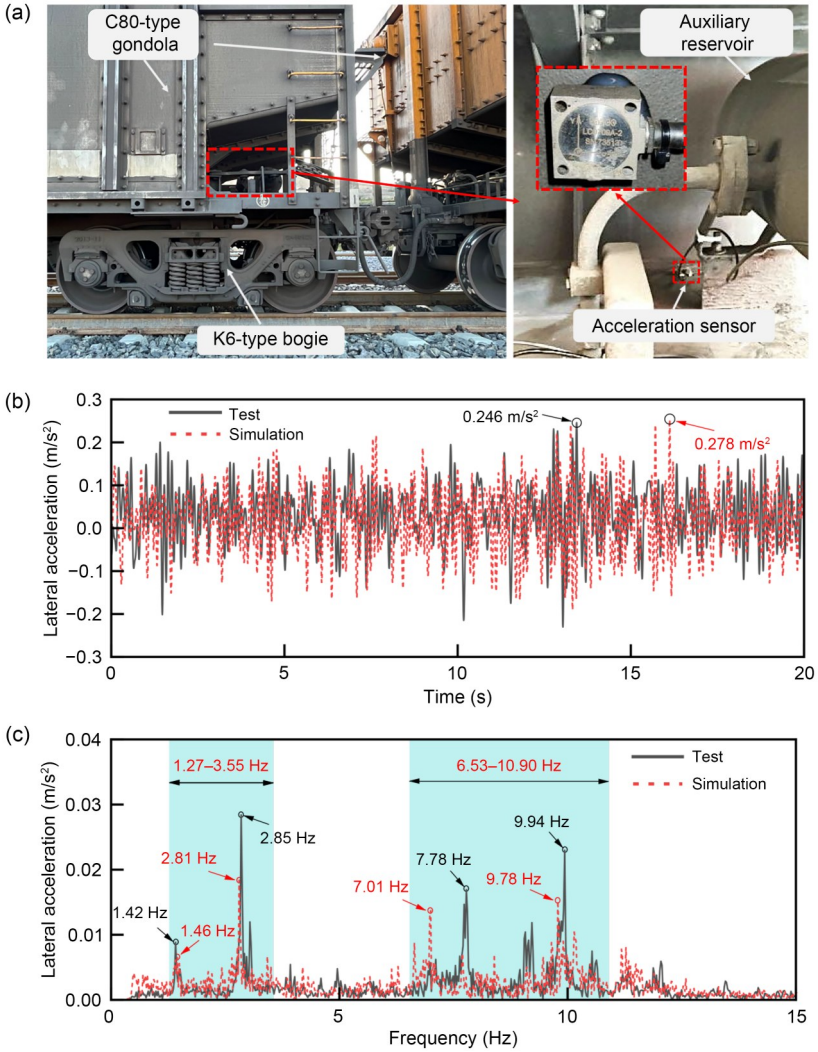

Fig. 6 Field test validation of acceleration: (a) installation location of the acceleration sensor in the field test; (b) time-domain acceleration in the simulation and the field test; (c) frequency-domain acceleration in the simulation and the field test

observed in the calculated high-frequency range (6.53–10.90 Hz). While different track irregularities can influence the frequency-domain response of the vehicle system, the natural frequencies of the vehicle itself essentially remain unchanged, and the corresponding vibration modes can still be effectively excited. According to previously calculated vibration mode results, the modes associated with the lateral vibration of the car body are lateral sway (1.46 Hz) and overturning (2.10 Hz). These results indicate that the dynamic model can accurately capture the lateral vibration characteristics of the car body. Overall, these results indicate that the established MBD model is suitable for simulating the dynamic behavior of trains passing through straight sections.

4 Simulation results

The simulation results of the freight trains primarily include time-averaged analysis of aerodynamic loads, transient flow field analysis, and dynamic responses.

4.1 Time-averaged analysis of aerodynamic load

Table 3 presents the time-averaged aerodynamic drag coefficient (C_x) and aerodynamic lateral force coefficient (C_y) for Gondolas 1–4. Cases 1–5 correspond to windbreak heights (H_w) of 0 m, 1.5 m, 2 m, 3 m, and 4 m, respectively. The time-averaged results for Cases 2–5 are calculated after the entire freight train has fully

entered the windbreak. Aerodynamic drag is defined as positive in the $-x$ direction, while lateral force is positive in the $-y$ direction. A more detailed description of the aerodynamic coefficient and safety index is given in the ESM.

For Case 1, since the train speed is lower than the crosswind speed, the C_x of the train without a windbreak is significantly smaller than the C_y. The C_y decreases sequentially from Gondola 1 to Gondola 4, showing an approximate linear relationship. For Cases 2–5, the C_y significantly decreases after the train fully enters the windbreak. Furthermore, the difference in C_y between different gondolas is small. When the H_w value is greater than 2 m, the direction of the lateral force changes from positive to negative.

The crosswind mainly affects the time-averaged overturning moment coefficient (C_{mx}) and the yaw moment coefficient (C_{mz}) of the train, as shown in Table 4. Compared to the no-windbreak condition, a H_w of 1.5 m increases the C_{mx} of the gondolas. When the H_w exceeds 1.5 m, the C_{mx} decreases as the H_w increases. The C_{mz} for Cases 2–5 significantly decreases, and when the H_w is greater than 2 m, Gondola 2 shows a relatively large C_{mz}. The relationship between the aerodynamic coefficient and the height of the windbreak wall is shown in the ESM.

Fig. 7 depicts the distribution of the time-averaged surface pressure coefficient at a height of z=3 m for Case 1. On the windward side, flow separation causes rapid changes in airflow velocity and significant pressure gradients at the edges of the car body. The distribution of positive pressure is generally consistent from Gondola 1 to Gondola 3, while the low-pressure region for Gondola 4 is primarily concentrated at the rear; this

Table 3 Time-averaged aerodynamic drag coefficient and aerodynamic lateral force coefficient of Gondolas 1–4

Case	Gondola 1		Gondola 2		Gondola 3		Gondola 4	
	C_x	C_y	C_x	C_y	C_x	C_y	C_x	C_y
1	1.78	20.99	1.85	18.89	1.82	17.32	1.37	14.47
2	1.22	1.33	1.07	1.16	1.23	0.87	2.03	1.64
3	1.18	−1.01	1.39	−1.40	0.88	−0.41	1.17	−0.59
4	2.03	−1.88	1.30	−1.44	0.43	−0.54	0.91	−1.22
5	2.44	−0.82	1.46	−1.57	0.82	−0.95	1.64	−1.41

Table 4 Time-averaged aerodynamic overturning moment coefficient and yaw moment coefficient of Gondolas 1–4

Case	Gondola 1		Gondola 2		Gondola 3		Gondola 4	
	C_{mx}	C_{mz}	C_{mx}	C_{mz}	C_{mx}	C_{mz}	C_{mx}	C_{mz}
1	0.92	−1.25	1.08	−0.86	0.92	−0.80	0.55	−1.30
2	1.27	0.10	1.35	−0.10	1.34	0.14	1.83	0.16
3	0.37	0.02	0.01	0.40	0.22	0.23	0.27	−0.05
4	−0.14	0.38	−0.22	0.52	−0.02	0.01	−0.14	−0.16
5	−0.68	0.20	−0.74	0.35	−0.19	0.25	−0.13	0.02

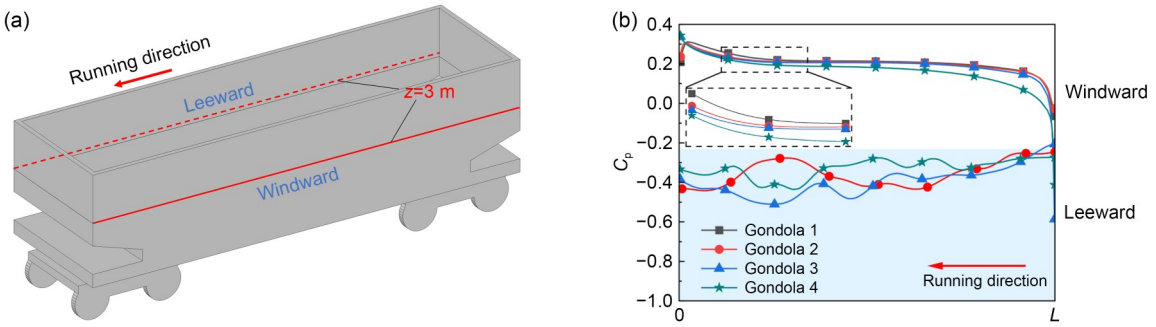

Fig. 7 (a) Monitoring lines of surface pressure coefficients; (b) distribution of the time-averaged pressure coefficient on the surface of gondolas

results in a smaller lateral force but larger reverse yaw moment. In contrast to the windward side, the flow field on the leeward side primarily shows a negative pressure distribution. The pressure coefficients on the leeward side fluctuate more significantly, with Gondola 1 experiencing a large negative pressure distribution, which leads to a larger side force. For Gondolas 2 and 3, the changes in pressure coefficients along the direction of the train movement are less obvious, resulting in smaller yaw moments.

4.2 Analysis of the instantaneous flow field

To more clearly illustrate the impact of differing windbreak height on the flow field around the freight car, Fig. 8 depicts the velocity line integral convolution on the lateral cross-section of Gondola 2 at t=3 s. When H_w is 1.5 m, the crosswind inflow accelerates towards the gondola after passing through the windbreak on the windward side. Due to the insufficient height of the windbreak, a portion of the high-speed airflow is obstructed by the side wall of the freight car, creating a large-scale vortex (V_1) near the wall, and generating small-scale vortices above and within the cavity of the gondola. A magnified view reveals that the flow slows down and the pressure increases upon contact with the side wall of the car, resulting in a larger overturning moment for the gondola compared to the non-windbreak condition. When H_w is increased to 2 m, the high-speed airflow is not obstructed by the side wall of the car, leading to the generation of more large-scale vortices, such as V_2 above the gondola. The flow between the windbreak and the gondola, as well as within the cavity, exhibits lower velocity. The velocity distribution near the side wall of the gondola is relatively uniform. As shown in Fig. 8, when H_w reaches 3 m, the number of small-scale vortices on the leeward side decreases, and a vortex V_3 forms above the leeward side of the gondola. The variation in flow velocity is minimal in the region between the gondola bottom and the windbreak. When H_w is increased further to 4 m, the crosswinds have little effect on the variation of the flow velocity around the gondola, and the vortex V_4 near the leeward internal wall grows.

The vortices on the leeward side and wake are the primary source of fluctuations in the aerodynamic loads of the train (Niu et al., 2022; Zhu et al., 2024). Taking Cases 2 and 5 as typical examples, we analyze the variations in pressure coefficient on the internal and outer walls of Gondola 2. From Fig. 9, it can be seen that the pressure distribution on the leeward outer wall is generally consistent between the two cases, with the principal differences concentrated on the windward outer wall and the leeward internal wall. In Case 2, due to the insufficient height of the windbreak, the flow impacts the upper part of the windward outer wall, resulting in a significant increase in the pressure coefficient (C_p=1.02). In Case 5, the flow passing through the windbreak and the windward outer wall forms large-scale vortices (as indicated by the velocity vectors), creating local low-pressure regions around and within the gondola, and resulting in a lower pressure coefficient on the leeward internal wall (C_p=−2.17). When the H_w is greater than or equal to 2 m, the crosswind flow primarily affects the internal flow field of the gondola, leading to larger magnitudes of the lateral force coefficient

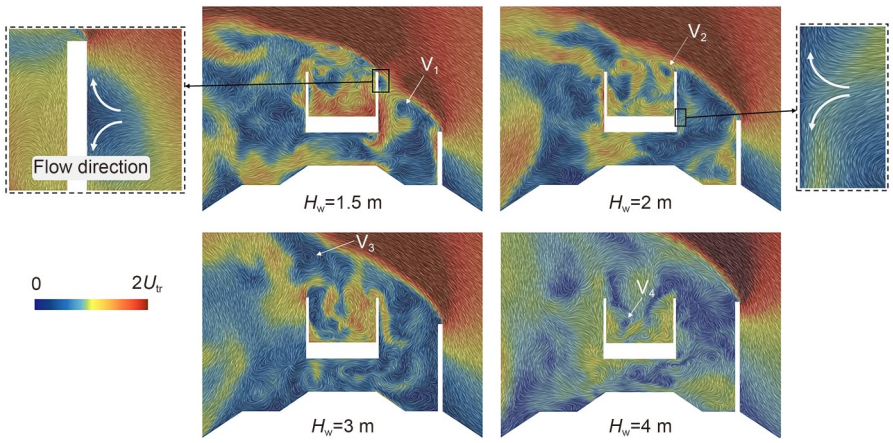

Fig. 8 Velocity line integral convolution on the lateral cross-section of Gondola 2 at t=3 s for Cases 2–5. U_{tr} is the speed of train. References to color refer to the online version of this figure

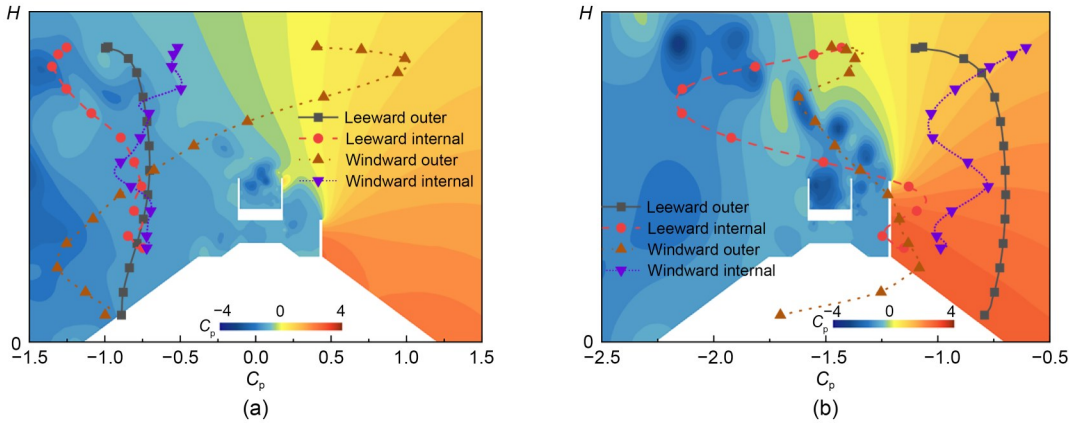

Fig. 9 Distribution of the surface pressure coefficient with height: (a) Case 2; (b) Case 5

and overturning moment. Additionally, the distribution of the streamline above the embankment on the leeward side and the distribution of turbulent kinetic energy are shown in the ESM.

4.3 Nonlinear dynamic response

In this section, the nonlinear dynamic response of the train under crosswind is analyzed from three aspects: the time-domain response, frequency-domain response, and statistical results. The aim is to evaluate the operational safety of the train with and without a windbreak. To mitigate the impact of initial disturbances on the accuracy of the dynamic response, the aerodynamic load is set to start at 1 s. Additionally, to reduce the dynamic impulse caused by the direct loading and unloading of aerodynamic loads, a loading process from 0 to 5 s and an unloading process from 10 to 15 s are applied. Figs. 10a and 10b illustrate the aerodynamic load curve of Case 3, showing linear variations in aerodynamic load during both the loading and unloading processes. When the vehicle enters the windbreak, a reduction in surface pressure on the front side occurs, while the rear side remains influenced by the crosswind. The yaw moment reaches a maximum at 7.11 s, when the front half of the vehicle enters the windbreak.

Figs. 10c and 10d illustrate the lateral and vertical wheel–rail forces of the first wheelset in Gondola 2. At 6.29 s, the wheelset enters the area behind the windbreak. Note that during the period of 5 to 6.29 s, when the train travels without a windbreak, there is minimal variation in the lateral and vertical wheel–rail forces. The action of the crosswind leads to significantly smaller lateral forces on the windward side compared to the leeward side. The overturning moment from the crosswind results in smaller vertical forces on the windward side compared to the leeward side. At the times of 5 s and 7.11 s, due to the aerodynamic force and yaw moment reaching their maximum values, significant dynamic impulses occur at these positions. The maximum lateral force fluctuation amplitude on the right side (leeward side) of the first wheelset is 26.65 kN, and the maximum vertical force fluctuation amplitude is 34.11 kN. Figs. 10e and 10f show the lateral and vertical accelerations of Gondola 2. The lateral acceleration reaches 3.42 m/s² at 5.34 s. After the entire train enters the windbreak, both the lateral and vertical accelerations significantly decrease.

The lateral wheelset force is the sum of the left and right lateral wheel–rail forces, and reflects the influence of aerodynamic load on the dynamic performance of the train. Fig. 10g shows the lateral forces of the first wheelset of Gondola 2 with different windbreaks. According to the previous analysis, because of the insufficient height of the windbreak, the overturning moment increases after the gondola enters the 1.5 m windbreak, causing the lateral wheelset force to increase. In contrast, the lateral wheelset force significantly decreases after the gondolas enter the 2 m and 4 m windbreaks, as shown in the enlarged section. Due to the low-pressure effect of the vortex inside the gondola when the vehicle is traveling behind the 3 m and 4 m windbreaks, the car body experiences an aerodynamic force opposite to the direction of the crosswind, and the negative values of the lateral wheelset force become larger, measuring 6.52 kN and 6.79 kN. Fig. 10h depicts the lateral wheelset forces of different gondolas. According to the results in Table 4, before the train enters the windbreak, the lateral wheelset force of

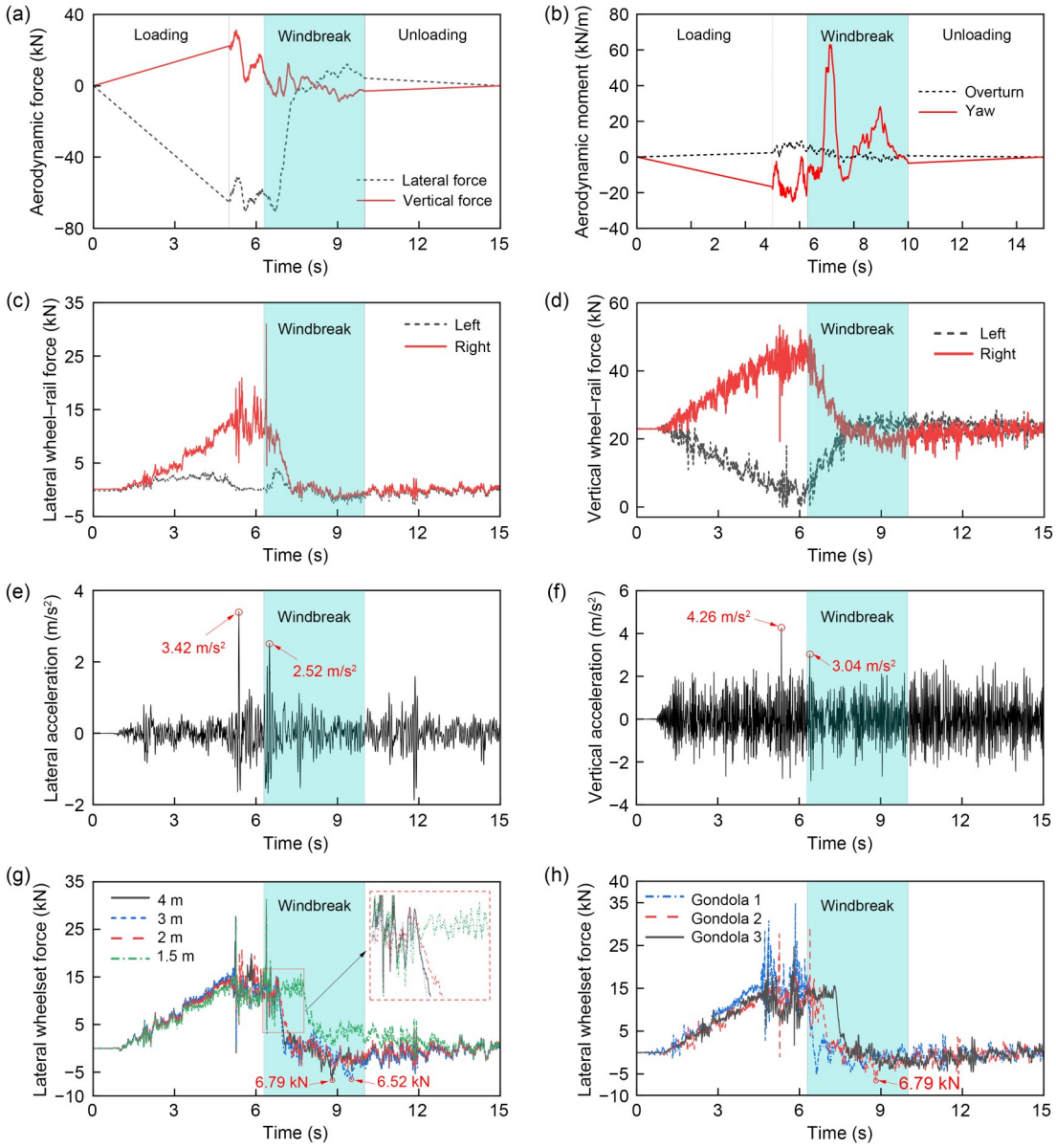

Fig. 10 Time-domain aerodynamic load and dynamic response: (a) aerodynamic force; (b) aerodynamic moment; (c) lateral wheel–rail force; (d) vertical wheel–rail force; (e) lateral acceleration; (f) vertical acceleration; (g) lateral forces of the first wheelset of Gondola 2 with different windbreaks; (h) lateral wheelset forces of different gondolas

Gondola 1 is the largest, due to the larger aerodynamic lateral force. As gondolas pass through the windbreak with a height of 4 m, the lateral wheelset force decreases significantly. Gondola 2 is subjected to a larger aerodynamic lateral force and overturning moment, and reaches a maximum lateral wheelset force in the reverse direction of 6.79 kN. The variation of vehicle attitude is analyzed in the ESM.

The frequency-domain responses of the lateral and vertical accelerations for each gondola under different conditions are shown in Fig. 11. Table 5 presents the frequencies of the car body vibration modes and dynamic responses. The vertical vibration of the car body is related to the bounce (20.73 Hz) and pitch (26.35 Hz), and thereby the frequency of the vertical acceleration closely aligns with the corresponding vibration mode. Furthermore, lateral vibrations are more pronounced in the low-frequency range compared to vertical vibrations. The low-frequency overturning vibration modes (2.10 Hz) corresponding to the lateral vibrations are also excited under crosswind loads. The maximum amplitude of lateral vibration corresponds to the frequencies

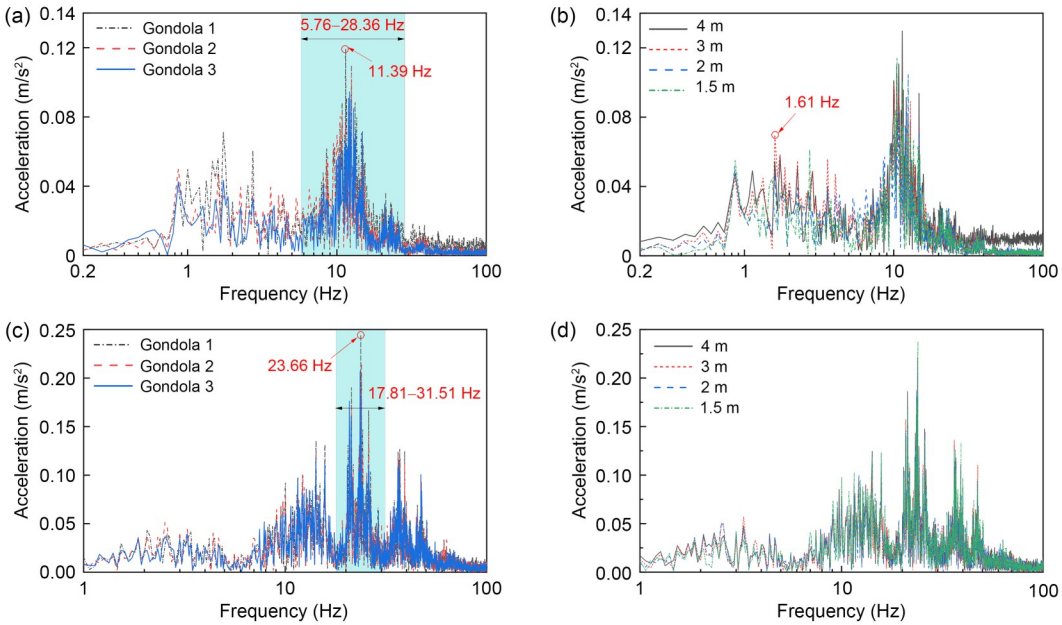

Fig. 11 Frequency-domain response of acceleration: (a) lateral acceleration of different gondolas; (b) lateral acceleration with different windbreaks; (c) vertical acceleration of different gondolas; (d) vertical acceleration with different windbreaks

Table 5 Frequency of the car body vibration mode and dynamic response

Vibration mode type of car body	Numerical frequency (Hz)	Dynamic response (Hz)
Lateral sway and overturning	1.33	1.61 (lateral acceleration)
Lateral sway and overturning	1.46	1.61 (lateral acceleration)
Overturning	2.10	1.61 (lateral acceleration)
Bounce	20.73	23.66 (vertical acceleration)
Pitch	26.35	23.66 (vertical acceleration)

of 11.39 Hz and 1.61 Hz, and is mainly concentrated in the range of 5.76 to 28.36 Hz. The amplitudes increase successively for Gondola 3, Gondola 2, and Gondola 1. In the frequency range below 5.76 Hz, windbreaks with heights of 1.5 m and 2 m effectively reduce the amplitude of Gondola 2, while windbreaks of 3 m and 4 m height result in larger amplitudes. According to the analysis of the vibration modes and transient flow field, this behavior can be attributed to the adverse pressure distribution caused by the vortices on the leeward side, which intensify the lateral force and overturning moment; this ultimately enhances the low-frequency vibration (1.61 Hz). The maximum amplitude of vertical vibration occurs at a frequency of 23.66 Hz, and is mainly concentrated in the range from 17.81 to 31.51 Hz. Notably, the influence of different gondolas and windbreak heights on the amplitude and frequency of vertical vibration is relatively weak.

The time-domain response results reveal the maximum values of safety indicators for train operation under varying windbreak heights. Among these indicators, the derailment coefficient (C_D), wheel unloading ratio (R), and overturning coefficient (C_O) are primarily associated with wheel–rail forces. These are important safety indicators for evaluating the risk of derailment and overturning under crosswinds. Looking at Fig. 12, one can see that both R and C_O exceed their limits in the absence of a windbreak under a 30 m/s crosswind. The established limits for C_D, R, and C_O are 1, 0.65, and 0.8, respectively (SAMR, 2019). When R reaches 1, the wheel–rail force on the windward side drops to 0, leaving the wheels on both sides susceptible to relative displacement and derailment. When the H_w value increases from 0 to 2 m, all safety indicators show a significant decrease. As H_w reaches or exceeds 2 m, all safety indicators meet the limits, and further increasing H_w causes no significant changes in safety indicators. Compared to the no-windbreak condition, a 2 m windbreak reduces the C_D, R, and C_O by 76%, 64%, and 81%, respectively. This analysis demonstrates that

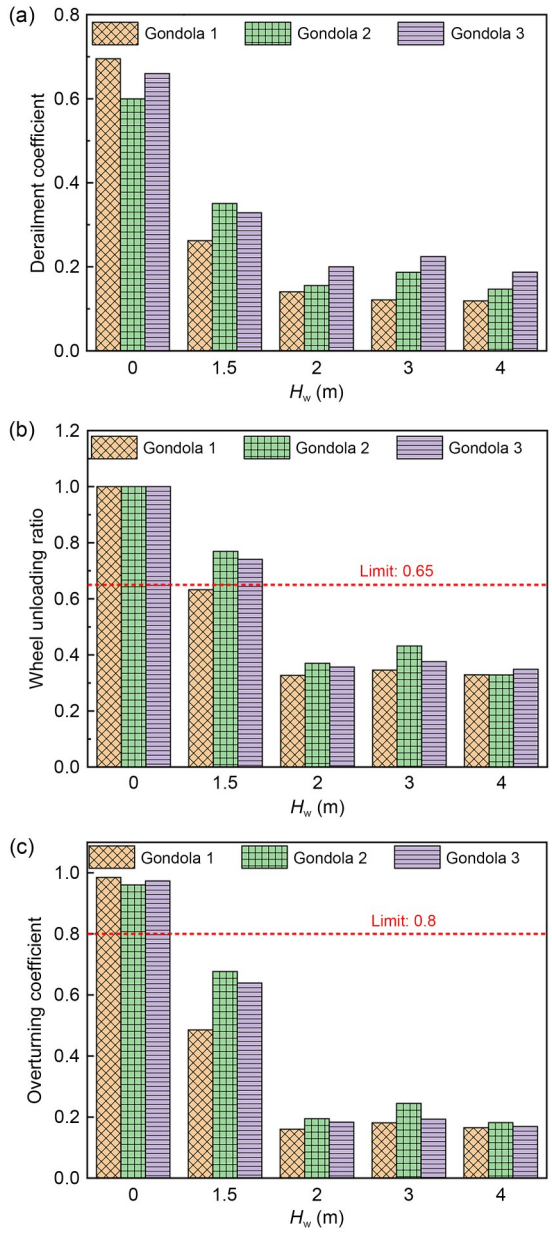

Fig. 12 Index of safety: (a) derailment coefficient (C_D); (b) wheel unloading ratio (R); (c) overturning coefficient (C_O)

a 2 m windbreak can effectively reduce aerodynamic loads and enhance the safety of train operation, while also considering economic factors.

5 Conclusions

The aerodynamic and dynamic characteristics of gondola train cars were investigated in this study. Time-averaged aerodynamic loads were numerically simulated under various conditions and analyzed using a 30 m/s crosswind. Additionally, the mechanism of influence for windbreak height on aerodynamic loads was revealed through analysis of the transient flow field. Finally, the nonlinear dynamic response of the train was studied and its operational safety was evaluated.

A windbreak of 2 m height was found to effectively shield the impact of crosswind flow on the sidewalls of the gondolas, significantly reducing the aerodynamic lateral force, yaw moment, and overturning moment. When the windbreak height exceeded 2 m, the flow field was primarily affected by the vortices within the gondola. Moreover, the lateral force and overturning moment resulted in a decrease in wheel–rail forces on the windward side, and an increase on the leeward side. When the height of the windbreak exceeded 2 m, vortices within the gondola induced an adverse pressure coefficient distribution (C_p=−2.17) on the leeward internal wall, amplifying both the lateral force and overturning moment of the car body. Frequency-domain analysis indicated that the vertical vibration of the car body is related to the bounce (20.73 Hz) and pitch (26.35 Hz), while the low-frequency overturning (2.10 Hz) vibration modes that correspond to the lateral vibrations are also excited under crosswind loads.

All safety indicators exceeded their limits without a windbreak. A 2 m windbreak can reduce the lateral acceleration, derailment coefficient C_D, wheel unloading ratio R, and overturning coefficient C_O of the train to acceptable levels. However, further increasing the windbreak height results in minimal improvements in safety indicators. Considering construction volume and cost-effectiveness, the installation of a single 2 m windbreak on the windward side can effectively reduce the aerodynamic loads, and the risk of derailment and overturning for unloaded freight trains. However, a few limitations of this study should be noted. For one, the operational environment of the train was simplified. The influences of curves, gradients, tunnels, and varying windbreak structures on the crosswind flow field and vehicle dynamics were not considered. Furthermore, both the train speed and wind speed were assumed to be constant, which deviates from real-world conditions to some extent. Additionally, the physical time of the numerical simulations was relatively short, and focused primarily on the process of the train entering and operating within the windbreak. In future research, we will further explore the influence of embankment height, vehicle type, and windbreak configuration on the lateral stability and operational safety of trains.

Acknowledgments

This work is supported by the National Natural Science Foundation of China (No. 52388102) and the Science and Technology Research and Development Program of China State Railway Group Co., Ltd. (No. N2024J039). The authors also thank the New Cornerstone Science Foundation through the XPLORER PRIZE.

Author contributions

Jiayuan SONG designed the research. Wentao HE processed the corresponding data. Jiayuan SONG wrote the first draft of the manuscript. Yanlin HU helped to organize the manuscript. Kaiyun WANG revised and edited the final version.

Conflict of interest

Jiayuan SONG, Wentao HE, Yanlin HU, and Kaiyun WANG declare that they have no conflict of interest.

References

Andersson E, Häggström J, Sima M, et al., 2004. Assessment of train-overturning risk due to strong cross-winds. *Proceedings of the Institution of Mechanical Engineers, Part F: Journal of Rail and Rapid Transit*, 218(3):213-223. https://doi.org/10.1243/0954409042389382

Cheli F, Corradi R, Rocchi D, et al., 2010. Wind tunnel tests on train scale models to investigate the effect of infrastructure scenario. *Journal of Wind Engineering and Industrial Aerodynamics*, 98(6-7):353-362. https://doi.org/10.1016/j.jweia.2010.01.001

Dai ZY, Li T, Zhang WH, et al., 2024. Investigation on aerodynamic characteristics of high-speed trains with shields beneath bogies. *Journal of Wind Engineering and Industrial Aerodynamics*, 246:105666. https://doi.org/10.1016/j.jweia.2024.105666

Flynn D, Hemida H, Baker C, 2016. On the effect of cross-winds on the slipstream of a freight train and associated effects. *Journal of Wind Engineering and Industrial Aerodynamics*, 156:14-28. https://doi.org/10.1016/j.jweia.2016.07.001

Gao GJ, Duan LL, 2011. Height of wind barrier on embankment of single railway line. *Journal of Central South University (Science and Technology)*, 42(1):254-259 (in Chinese).

Gao GJ, Li P, 2011. Runing stability of container car in Qinghai—Tibet railway line. *Journal of Central South University* (*Science and Technology*), 42(2):533-538 (in Chinese).

Gao HR, Liu TH, Chen XD, et al., 2024. Flow characteristics induced by a multiform windbreak in complex terrains with and without a train: a simplified method for calculating aerodynamic loads. *Physics of Fluids*, 36(12):125115. https://doi.org/10.1063/5.0236039

Gao HR, Liu TH, Chen XD, et al., 2025. Aerodynamic and dynamic behaviour of a train in cutting-viaduct-cutting sections with windbreaks in complex terrains under cross-winds: key factors. *Engineering Structures*, 328:119728. https://doi.org/10.1016/j.engstruct.2025.119728

Ge X, Ling L, Guo LR, et al., 2022. Dynamic derailment simulation of an empty wagon passing a turnout in the through route. *Vehicle System Dynamics*, 60(4):1148-1169. https://doi.org/10.1080/00423114.2020.1849744

Golovanevskiy VA, Chmovzh VV, Girka YV, 2012. On the optimal model configuration for aerodynamic modeling of open cargo railway train. *Journal of Wind Engineering and Industrial Aerodynamics*, 107-108:131-139. https://doi.org/10.1016/j.jweia.2012.03.035

Guo ZJ, Liu TH, Liu Z, et al., 2021. An IDDES study on a train suffering a crosswind with angles of attack on a bridge. *Journal of Wind Engineering and Industrial Aerodynamics*, 217:104735. https://doi.org/10.1016/j.jweia.2021.104735

Hashmi SA, Hemida H, Soper D, 2019. Wind tunnel testing on a train model subjected to crosswinds with different windbreak walls. *Journal of Wind Engineering and Industrial Aerodynamics*, 195:104013. https://doi.org/10.1016/j.jweia.2019.104013

He WT, Hu YL, Ge X, et al., 2025. Research on operational safety of empty gondola cars in freight trains subjected to crosswind. *Engineering Mechanics*, 42(1):249-258 (in Chinese). https://doi.org/10.6052/j.issn.1000-4750.2022.10.0919

Hu X, Deng ZG, Zhang WH, 2021. Effect of cross passage on aerodynamic characteristics of super-high-speed evacuated tube transportation. *Journal of Wind Engineering and Industrial Aerodynamics*, 211:104562. https://doi.org/10.1016/j.jweia.2021.104562

Hu YL, Ge X, Ling L, et al., 2025. Dynamic performance of a high-speed train exiting a tunnel under crosswinds. *Journal of Zhejiang University-SCIENCE A*, 26(1):21-35. https://doi.org/10.1631/jzus.A2300610

Li C, Burton D, Kost M, et al., 2017. Flow topology of a container train wagon subjected to varying local loading configurations. *Journal of Wind Engineering and Industrial Aerodynamics*, 169:12-29. https://doi.org/10.1016/j.jweia.2017.06.011

Li NX, Li T, Dai ZY, et al., 2024. Effect of streamlined nose length on aerodynamic performance of high-speed train with a speed of 400 km/h. *Journal of Zhejiang University-SCIENCE A*, 25(7):525-540. https://doi.org/10.1631/jzus.A2300301

Li T, Qin D, Zhang JY, 2019. Effect of RANS turbulence model on aerodynamic behavior of trains in crosswind. *Chinese Journal of Mechanical Engineering*, 32(1):85. https://doi.org/10.1186/s10033-019-0402-2

Li T, Liang H, Zhang J, et al., 2023. Numerical study on aerodynamic resistance reduction of high-speed train using vortex generator. *Engineering Applications of Computational Fluid Mechanics*, 17(1):e2153925. https://doi.org/10.1080/19942060.2022.2153925

Li T, Li YF, Wei L, et al., 2025. Comparative study on lateral vibration characteristics of the head and tail cars of high-speed trains under unsteady aerodynamic loadings. *Vehicle System Dynamics*, 63(3):518-536. https://doi.org/10.1080/00423114.2024.2346574

Liang H, Sun Y, Li T, et al., 2023. Influence of marshalling

length on aerodynamic characteristics of urban emus under crosswind. *Journal of Applied Fluid Mechanics*, 16(1): 9-20.
https://doi.org/10.47176/jafm.16.01.1338

Liu TH, Wang L, Gao HR, et al., 2022. Research progress on train operation safety in Xinjiang railway under wind environment. *Transportation Safety and Environment*, 2(4): tdac005.
https://doi.org/10.1093/tse/tdac005.

Maleki S, Burton D, Thompson MC, 2017. Assessment of various turbulence models (ELES, SAS, URANS and RANS) for predicting the aerodynamics of freight train container wagons. *Journal of Wind Engineering and Industrial Aerodynamics*, 170:68-80.
https://doi.org/10.1016/j.jweia.2017.07.008

Maleki S, Burton D, Thompson MC, 2019. Flow structure between freight train containers with implications for aerodynamic drag. *Journal of Wind Engineering and Industrial Aerodynamics*, 188:194-206.
https://doi.org/10.1016/j.jweia.2019.02.007

Maleki S, Burton D, Thompson MC, 2020. On the flow past and forces on double-stacked wagons within a freight train under cross-wind. *Journal of Wind Engineering and Industrial Aerodynamics*, 206:104224.
https://doi.org/10.1016/j.jweia.2020.104224

Menter FR, 1994. Two-equation eddy-viscosity turbulence models for engineering applications. *AIAA Journal*, 32(8): 1598-1605.
https://doi.org/10.2514/3.12149

Mohebbi M, Rezvani MA, 2019. Analysis of the effects of lateral wind on a high speed train on a double routed railway track with porous shelters. *Journal of Wind Engineering and Industrial Aerodynamics*, 184:116-127.
https://doi.org/10.1016/j.jweia.2018.11.011

Mohebbi M, Ma Y, Mohebbi R, 2025. Enhancing high-speed train stability: unraveling the influence of sloping crosswind shields on aerodynamic characteristic. *Engineering Structures*, 326:119569.
https://doi.org/10.1016/j.engstruct.2024.119569

Moukalled F, Mangani L, Darwish M, 2016. The Finite Volume Method in Computational Fluid Dynamics. Springer, Cham, Germany.
https://doi.org/10.1007/978-3-319-16874-6

Niu JQ, Zhou D, Liang XF, 2018. Numerical investigation of the aerodynamic characteristics of high-speed trains of different lengths under crosswind with or without windbreaks. *Engineering Applications of Computational Fluid Mechanics*, 12(1):195-215.
https://doi.org/10.1080/19942060.2017.1390786

Niu JQ, Zhang YC, Li R, et al., 2022. Aerodynamic simulation of effects of one- and two-side windbreak walls on a moving train running on a double track railway line subjected to strong crosswind. *Journal of Wind Engineering and Industrial Aerodynamics*, 221:104912.
https://doi.org/10.1016/j.jweia.2022.104912

Noguchi Y, Suzuki M, Baker C, et al., 2019. Numerical and experimental study on the aerodynamic force coefficients of railway vehicles on an embankment in crosswind. *Journal of Wind Engineering and Industrial Aerodynamics*, 184: 90-105.
https://doi.org/10.1016/j.jweia.2018.11.019

NRA (National Railway Administration of the People's Republic of China), 2016. Code for Design of Railway Earth Structure, TB10001-2016. National Standards of the People's Republic of China (in Chinese).

NRA (National Railway Administration of the People's Republic of China), 2017. Code for Design of Railway Line, TB10098-2017. National Standards of the People's Republic of China (in Chinese).

Pan YM, Li ZP, Wang XF, et al., 2025. Effect of side track height on aerodynamic characteristics of a high-speed high-temperature superconducting maglev train under crosswind. *Journal of Zhejiang University-SCIENCE A*, 26(10):983-996.
https://doi.org/10.1631/jzus.A2400555

Quazi A, Crouch T, Bell J, et al., 2023. A field study on the aerodynamics of freight trains with different stacking configurations. *Journal of Wind Engineering and Industrial Aerodynamics*, 232:105245.
https://doi.org/10.1016/j.jweia.2022.105245

RAIB (Rail Accident Investigation Branch), 2009. Detachment of Containers from Freight Wagons Near Cheddington and Hardendale, 1 March 2008. Rail Accident Report, RAIB, UK.

SAMR (State Administration for Market Regulation), 2019. Specification for Dynamic Performance Assessment and Testing Verification of Rolling Stock, GB/T5599-2019. National Standards of the People's Republic of China (in Chinese).

Shur ML, Spalart PR, Strelets MK, et al., 2008. A hybrid RANS-LES approach with delayed-DES and wall-modelled LES capabilities. *International Journal of Heat and Fluid Flow*, 29(6):1638-1649.
https://doi.org/10.1016/j.ijheatfluidflow.2008.07.001

Sun Z, Dai HY, Gao H, et al., 2019. Dynamic performance of high-speed train passing windbreak breach under unsteady crosswind. *Vehicle System Dynamics*, 57(3):408-424.
https://doi.org/10.1080/00423114.2018.1469777

Sun Z, Dai HY, Hemida H, et al., 2020. Safety of high-speed train passing by windbreak breach with different sizes. *Vehicle System Dynamics*, 58(12):1935-1952.
https://doi.org/10.1080/00423114.2019.1657909

Suzuki M, Tanemoto K, Maeda T, 2003. Aerodynamic characteristics of train/vehicles under cross winds. *Journal of Wind Engineering and Industrial Aerodynamics*, 91(1-2):209-218.
https://doi.org/10.1016/S0167-6105(02)00346-X

Tian HQ, 2015. Determination method of load balance ranges for train operation safety under strong wind. *Journal of Central South University*, 22(3):1146-1154.
https://doi.org/10.1007/s11771-015-2627-2

Wang G, Li QZ, Liu Y, 2021. IDDES method based on differential Reynolds-stress model and its application in bluff body turbulent flows. *Aerospace Science and Technology*, 119:107207.
https://doi.org/10.1016/j.ast.2021.107207

Wen JC, Li Q, Lu ZG, 2024. Safety of an express freight train running over a bridge in crosswind. *Proceedings of the Institution of Mechanical Engineers, Part F: Journal of Rail and Rapid Transit*, 238(1):89-101. https://doi.org/10.1177/09544097231192716

Xue RD, Xiong XH, Chen G, et al., 2025. Numerical comparison of aerodynamic performance between stationary and moving trains with varied-height windbreak wall under crosswind. *Alexandria Engineering Journal*, 110:540-556. https://doi.org/10.1016/j.aej.2024.10.050

Yang F, Liu TH, Shi ZL, et al., 2021. Influence of height of earth embankment type windbreak wall on flow field characteristics and catenary wind-induced displacement. *Engineering Applications of Computational Fluid Mechanics*, 15(1): 672-691. https://doi.org/10.1080/19942060.2021.1910573

Zhang D, Guo ZH, Ni YQ, et al., 2023. Correlation between cargo properties and train overturning safety for a high-speed freight train under strong winds. *Engineering Applications of Computational Fluid Mechanics*, 17(1):221308. https://doi.org/10.1080/19942060.2023.2221308

Zhang J, Liang XF, Liu TH, et al., 2011. Optimization research on aerodynamic shape of passenger car body with strong crosswind. *Journal of Central South University (Science and Technology)*, 42(11):3578-3584 (in Chinese).

Zhang QY, Zhou SQ, Xu G, et al., 2024. Integrated CFD and MBD methods for dynamic performance analysis of a high-speed train transitioning through varied windbreak corridor designs. *Journal of Wind Engineering and Industrial Aerodynamics*, 250:105755. https://doi.org/10.1016/j.jweia.2024.105755

Zhao L, Yang WC, Liu YK, et al., 2024. Effects of windbreak types on aerodynamics of high-speed trains traversing from flat ground to semi-cutting and semi-embankment under crosswinds. *Physics of Fluids*, 36(7):075115. https://doi.org/10.1063/5.0212334

Zhou D, Yu DZ, Wu LL, et al., 2023. Numerical investigation of the evolution of aerodynamic behaviour when a high-speed train accelerates under crosswind conditions. *Alexandria Engineering Journal*, 72:51-66. https://doi.org/10.1016/j.aej.2023.03.064

Zhu FT, Xie JW, Lv DZ, et al., 2024. Transient aerodynamic behavior of a high-speed Maglev train in plate braking under crosswind. *Physics of Fluids*, 36(3):035133. https://doi.org/10.1063/5.0189686

Zhuang YQ, Lu XY, 2015. Numerical investigation on the aerodynamics of a simplified high-speed train under crosswinds. *Theoretical and Applied Mechanics Letters*, 5(5):181-186. https://doi.org/10.1016/j.taml.2015.06.001

Electronic supplementary materials

Sections S1–S6; Table S1; Figs. S1–S7